JOURNAL OF SPACECRAFT AND ROCKETS
Vol. 43, No. 2, March–April 2006

Mars Science Laboratory Experimental Aerothermodynamics with Effects of Cavities and Control Surfaces

Derek S. Liechty,* Brian R. Hollis,† and Karl T. Edquist‡
NASA Langley Research Center, Hampton, Virginia 23681

Preliminary designs of the Mars Science Laboratory required it to be attached through its aeroshell to the main spacecraft bus, thereby producing cavities in the heat shield. Several configurations were considered experimentally for the Mars Science Laboratory, which have a Viking aeroshell heritage and provide the lift to drag required for precision landing. To study the effects of the cavities and control surfaces on the heating levels experienced by the heat shield, an experimental aeroheating investigation was performed at the NASA Langley Research Center in the 20-Inch Mach 6 Air Tunnel. Three configurations were studied experimentally. The first configuration was the baseline without any control surface. The last two include a blended tab control surface and a blended shelf control surface. The effects of Reynolds number, angle of attack, and cavity size and location on aeroheating levels and distributions were determined for each configuration and are presented. To aid the interpretation of the effects of the cavities, laminar, thin-layer Navier–Stokes flowfield solutions were performed for the baseline configuration and were then postprocessed to calculate relevant boundary-layer properties. It was found that the effect of the cavities varied with angle of attack, freestream Reynolds number, and cavity size and location. The presence of a cavity raised local heating rates by as much as 250% and the downstream heating rates by as much as 325% as a result of boundary-layer transition. Forebody cavities had no effect on afterbody heating, and the presence of control surfaces decreased leeward afterbody heating slightly.

Nomenclature

H = enthalpy, J/kg
h = heat-transfer coefficient, $q/(H_{\text{aw}} - H_w)$, where $H_{\text{aw}} = H_{t,2}$, kg/m^2/s
L = length of vehicle from nose to base, m
M = Mach number
p = pressure, Pa
q = surface heat-transfer rate, W/m^2
R = model reference radius, m
R_b = model base radius, m
R_{cs} = model radius from symmetry axis to control surface corner, m
R_n = model nose radius, m
R_s = model shoulder radius, m
Re = unit Reynolds number, 1/m
r = radial distance from symmetry axis, m
s = distance along surface from cavity center, m
t = control surface thickness, m
U = velocity magnitude, m/s
w = cavity diameter, m
z = distance along symmetry axis from nose, m
α = angle of attack, deg
β = angle control surface makes with symmetry axis, deg
γ = ratio of specific heats
δ = boundary-layer height, m
ζ = second afterbody angle, deg
η = body half-angle, deg
Θ = momentum thickness, $\int(\rho u/\rho_e u_e)(1 - u/u_e)\,\mathrm{d}y$, m
θ = cavity orientation angle, deg
ξ = first afterbody cone angle, deg
ρ = density, kg/m^3
τ = angle from the centerline to where control surface begins tapering toward vehicle, deg
ϕ = model orientation angle, deg
χ = angle from centerline to where control surface blends to vehicle, deg

Subscripts

aw = adiabatic wall conditions
D = based on model diameter
e = boundary-layer-edge conditions
FR = Fay–Riddell, stagnation-point, reference heating condition
fs = full-scale dimensions
S = based on blended shelf model
T = based on blended tab model
$t,1$ = reservoir conditions
$t,2$ = stagnation conditions behind a normal shock
w = wall conditions
∞ = freestream static conditions

Introduction

THE next generation of Mars landers[1] is being designed to enable precision landings at specific locations of particular scientific interest. The first-generation entry, descent, and landing systems, such as Viking and Pathfinder, achieved successful landings on Mars, but were limited in accuracy to landing sites on the order of hundreds of kilometers. The second-generation landers, or smart landers, will provide scientists with the opportunity to select a particular region of interest and land within 3 km of the intended target.

Preliminary designs[1] (2007) of the Mars Science Laboratory (2007 MSL), which was originally known as the Mars Smart Lander, required that it be attached to the main spacecraft bus by way of six structural inserts that pass through the forebody heat shield (Fig. 1; these designs have since been rejected in part because of this study). When the lander is separated from the spacecraft bus prior to entry into the Martian atmosphere, the bolts are severed and retracted,

Received 10 October 2002; revision received 1 August 2004; accepted for publication 1 February 2005.

*Aerospace Technologist, Aerothermodynamics Branch, Aerodynamics, Aerothermodynamics, and Acoustics Competency.
†Aerospace Technologist, Aerothermodynamics Branch, Aerodynamics, Aerothermodynamics, and Acoustics Competency. Senior Member AIAA.
‡Aerospace Technologist, Vehicle Analysis Branch, Aerospace Systems Concepts and Analysis Competency. Senior Member AIAA.

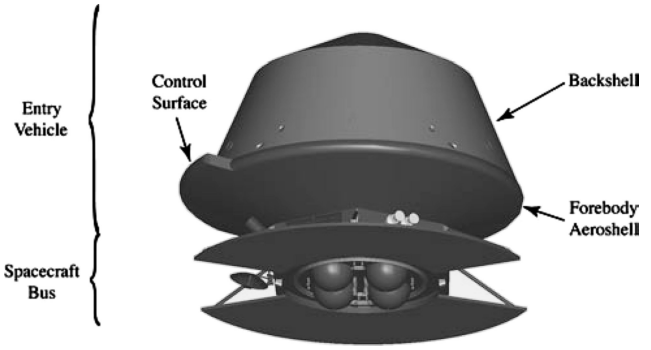

Fig. 1 2007 MSL cruise configuration.

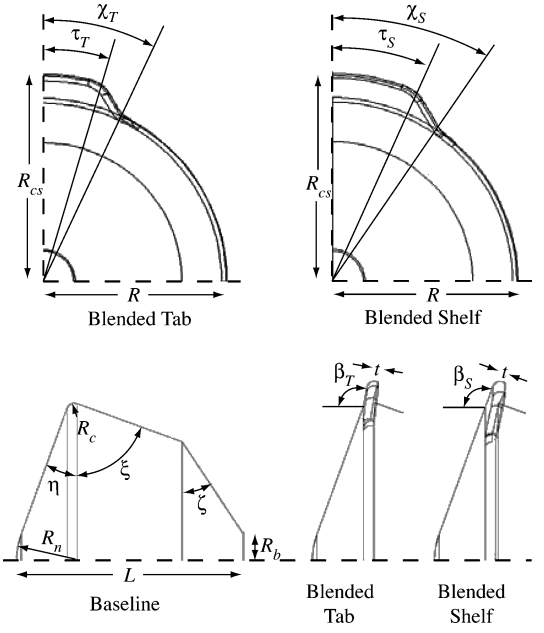

Fig. 2 2007 MSL geometries for the baseline, blended tab, and blended shelf configurations.

which leaves cavities in the forebody heat shield. The presence of these cavities in the heat shield during entry can result in high, localized heating at the downstream edge of the cavities because of flow separation and reattachment within the cavities and can be accompanied by a heating augmentation downstream of the cavities as a result of a change in the state of the boundary layer from laminar to transitional or turbulent. A similar design was employed for the Genesis Sample Return Capsule (GSRC),[2] which also included forebody heat-shield cavities, but there are several significant differences between the two vehicles. First, the forebody half-angle of the GSRC is different than the 2007 MSL. Also, the 2007 MSL was being designed to enter the Martian atmosphere at an angle of attack of 16 deg (which has since been changed to 11 deg), whereas the GSRC is to enter at 0-deg angle of attack.

As described in Ref. 1, the baseline 2007 configuration of the Mars Science Laboratory aeroshell (which has no control surface) provided a low ballistic coefficient for a given vehicle mass, a lift-to-drag ratio of 0.18, and had significant flight heritage (e.g., Viking). However, different aeroshell configurations were considered to meet the lift-to-drag requirement of 0.22 to 0.25 for precision landing. The baseline concept is capable of achieving these values of lift to drag by using ballast to provide a radial center-of-gravity offset so that the vehicle trims at an angle of attack. The ballast required to achieve the radial c.g. offset, however, is not insignificant.

In an attempt to save weight, tab and shelf configurations (Fig. 2) were investigated for application to the smart lander. The tab is inclined into the flow with respect to the forebody, while the shelf is an extension of the forebody. Tab concepts were investigated[3] as early as 1961 and considered again for the cancelled Mars Surveyor 2007 Precision Lander mission. Both the tab and shelf concepts can be sized to achieve the required lift-to-drag ratio of 0.22–0.25 at an angle of attack of approximately 16 deg. The advantage of the tab concepts compared to the shelf concepts is that the tabs can be smaller, because of the higher pressure produced on the tab. The disadvantage of the tab concepts, however, is elevated heating levels caused by the compression surface. A screening was performed of several tab configurations in the Langley Research Center (LaRC) 20-Inch Mach 6 CF_4 Tunnel to assess the aeroheating environments. From these results and computational studies[4,5] to optimize the shape of the tab, the current blended tab configuration was selected. The current blended shelf configuration was similarly optimized.[4,5]

The goal of the present study was to determine experimentally the aeroheating environment of the vehicle and control surfaces as well as how the cavities affected the heating levels on the forebody, afterbody, and control surfaces of the 2007 MSL. Tests were conducted at nominal conditions of Mach 6 in air (perfect gas; $\gamma \approx 1.4$) with freestream Reynolds numbers from 6.89×10^6/m to 23.95×10^6/m, resulting in Reynolds numbers based on diameter of 8.75×10^5 to 3.04×10^6. A range of angles of attack from 0 to 20 deg was studied. These conditions resulted in boundary-layer-edge conditions similar to those found in flight.[6] Three nominal cavity sizes were tested at two radial locations. Discrete trips were also placed upstream of the control surfaces in selected runs to transition the flow from laminar to turbulent to compare to the effects of the cavities. To complement the measurements made in the wind tunnel, laminar, thin-layer Navier–Stokes flowfield solutions generated using the Langley Aerothermodynamic Upwind Relaxation Algorithm[7,8] (LAURA) were postprocessed to calculate boundary-layer height, momentum thickness, edge Mach number, and streamwise pressure gradients. Only a qualitative discussion of boundary-layer properties will be included in this report. Corresponding computations and boundary-layer transition correlations for this study are presented in the companion paper by Hollis and Liechty[9] and for flight conditions by Edquis and Loomis.[6]

Experimental Methods

Test Facility

Aeroheating tests were conducted in the NASA Langley 20-Inch Mach 6 Air Tunnel. This is a blowdown facility in which heated, dried, and filtered air is used as the test gas. The tunnel has a two-dimensional, contoured nozzle that opens into a 0.5207×0.508 m test section. The tunnel is equipped with a bottom-mounted injection system that can transfer a model from the sheltered model box to the tunnel centerline in less than 0.5 s. Run times of up to 15 min are possible in this facility, although for the current aeroheating study run times of only a few seconds were required. The nominal reservoir conditions of this facility are stagnation pressures of 206.8 to 3447.4 kPa with stagnation temperatures of 422.2 to 555.5 K, which very nearly produce perfect gas ($\gamma \approx 1.4$) freestream flows with Mach numbers between 5.8 and 6.1 and Reynolds numbers of 1.64×10^6/m to 23.95×10^6/m. This results in values of Re_D of 2.08×10^5 to 3.04×10^6 for a 0.127-m-diam model. A comparison of the values of Re_D that the vehicle will see in flight with the range of Re_D the test facility is capable of achieving is shown in Fig. 3. The nominal flow conditions for these tests can be seen in Table 1. A more detailed description of this facility is presented in Ref. 10.

Phosphor Thermography Technique

Global surface heating distributions were calculated using the digital optical measurement method of two-color, relative-intensity, phosphor thermography.[11–14] Ceramic wind-tunnel models are coated with a phosphor compound that fluoresces in two separate regions (green and red) of the visible light spectrum. During a wind-tunnel run, the phosphor-coated model is illuminated by ultraviolet (UV) light sources, and the resulting fluorescent intensity of the model is recorded and digitized through a color charge-coupled-device camera. The fluorescent intensity is dependent on both the intensity of the incident UV light and the local model surface temperature. The UV intensity dependence is removed by taking the

Table 1 Flow conditions for the Langley 20-Inch Mach 6 Air Tunnel

Re_∞, 1/m	Re_D	M_∞	T_∞, K	ρ_∞, kg/m^3	U_∞, m/s	h_{FR}, kg/m^2/s	q_{FR}, W/cm^2
6.89×10^6	8.75×10^5	5.95	62.0	3.35×10^{-2}	938.6	0.283	5.70
8.53×10^6	1.08×10^6	5.97	62.2	4.05×10^{-2}	943.0	0.313	6.45
9.84×10^6	1.25×10^6	5.98	62.2	4.62×10^{-2}	944.4	0.335	6.95
1.12×10^7	1.42×10^6	5.99	61.6	5.29×10^{-2}	940.1	0.356	7.25
1.38×10^7	1.75×10^6	6.00	61.3	6.41×10^{-2}	940.4	0.392	7.95
1.51×10^7	1.92×10^6	6.01	63.5	7.25×10^{-2}	958.5	0.427	9.48
1.67×10^7	2.12×10^6	6.02	63.4	7.92×10^{-2}	958.7	0.446	9.92
1.90×10^7	2.41×10^6	6.03	62.8	8.99×10^{-2}	955.6	0.474	10.40
2.40×10^7	3.05×10^6	6.06	62.3	1.13×10^{-1}	954.6	0.529	11.50

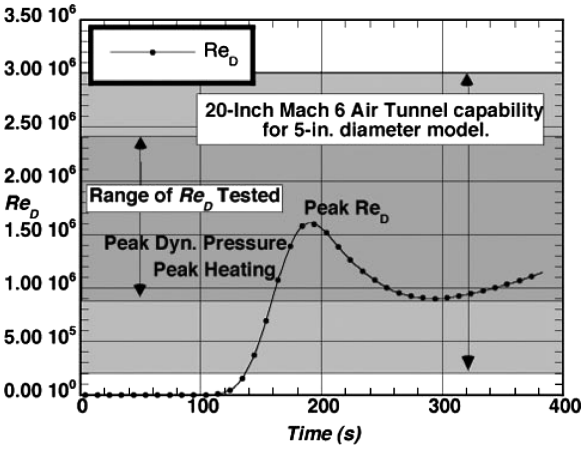

Fig. 3 Flight Re_D through a representative trajectory with 20-Inch Mach 6 Air Tunnel capability.

ratio of the green to red intensity images, from which surface temperature distributions can be determined through prior calibrations. Images are acquired before the wind-tunnel run and after injection of the model to the tunnel centerline during a run. Global heat-transfer distributions are then computed from these temperature data using one-dimensional, constant heat-transfer coefficient conduction theory.[14]

Test Model Description

To manufacture ceramic test models, rapid-prototype, stereolithographic resin models were first fabricated based on surface geometry definitions in electronic data files. Wax molds of the resin models were made, and then a patented[15] silica ceramic slip casting technique was used to form ceramic shells of the models. The shells were then backfilled with a hydraulically setting magnesia ceramic for strength and support. Finally, the models were coated with a mixture of phosphors suspended in a silica-based colloidal binder.

The cast ceramic aeroheating models were 0.127-m-diam, 0.0314-scale representations of the 4.05-m-diam Mars Science Laboratory aeroshell. Three configurations were considered in this study. First was the baseline configuration that had no control surface. The dimensions of the proposed baseline 2007 MSL aeroshell (full scale and test model) are shown in Table 2. Next, the blended tab configuration had the same dimensions as the baseline configuration, but a control surface was added at the corner, which was inclined 10 deg from the forebody heat shield. The dimensions of the proposed blended tab 2007 MSL aeroshell are listed in Table 3. Finally, the blended shelf configuration, which also had the same dimensions as the baseline configuration, had a control surface added at the corner, which is an extension of the 70-deg forebody half-angle. The dimensions of the proposed blended shelf 2007 MSL aeroshell are also shown in Table 3.

Four versions of the baseline configuration 2007 MSL will be discussed in this report. The first of these models was a baseline configuration model without any forebody cavities. The next three models

Table 2 Parameters for 2007 MSL geometry

Parameter	Full scale	Test model
R, m	2.0249	0.0635
R_n, m	0.9853	0.0309
R_s, m	0.0988	0.0031
R_b, m	0.3543	0.0111
L, m	2.9088	0.0913
η, deg	20.0	20.0
ξ, deg	70.0	70.0
ζ, deg	33.6	33.6

Table 3 Parameters for 2007 MSL control surface configuration

Parameter	Blended tab	Blended shelf
R_{cs}, m	0.0718	0.0718
t, m	0.0042	0.0042
β, deg	60.00	70.00
χ, deg	23.05	30.11
τ, deg	15.99	21.88

Table 4 Cavity numbering system for the 2007 MSL

Cavity number	r/R	w_{fs}, m
1	0.70	0.076
2	0.70	0.056
3	0.70	0.038
4	0.41	0.076
5	0.41	0.056
6	0.41	0.076

were the 2007 MSL cavity parametric models. They had a total of six cavities each located at 60-deg increments apart around the forebody (Fig. 4). Each cavity had a different radial location/diameter combination in an attempt to reduce the total number of runs required. (If each cavity on a model would have been the same, six times the number of runs would have been required for the same amount of data.) Each of the six cavities has been given a number (Table 4, Fig. 4). The forebody would have six cavities of the same size and radial location spaced at 60-deg increments, although the final size and locations were not fixed for the flight vehicle.

To identify the cavity locations as model orientation changed, two angles were defined. First, the model orientation angle ϕ is defined as 0 deg when cavity 1 is on the vertical upright in an image and increases as the model is rotated counterclockwise (Fig. 4). The second angle θ is the cavity orientation angle measured clockwise from the vertical upright in an image ($\theta = 0$ deg on the vertical upright regardless of the value of ϕ).

Smooth models (without cavities) of each control surface configuration were fabricated along with three cavity versions for the blended tab configuration (see Fig. 5 and Table 3). All cavities for the blended tab configuration were located at $r/R = 0.41$ and were the largest diameter studied from the baseline configuration. The

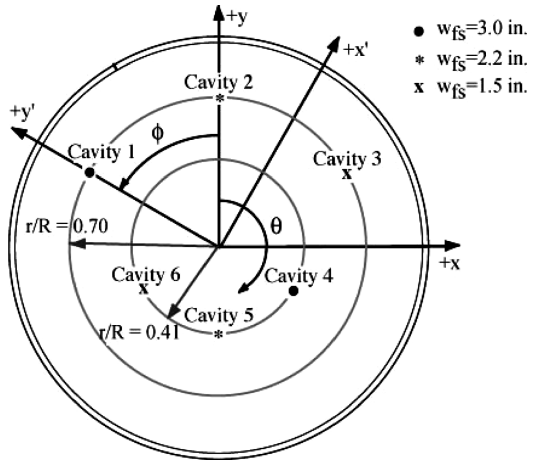

Fig. 4 2007 MSL model and cavity orientation.

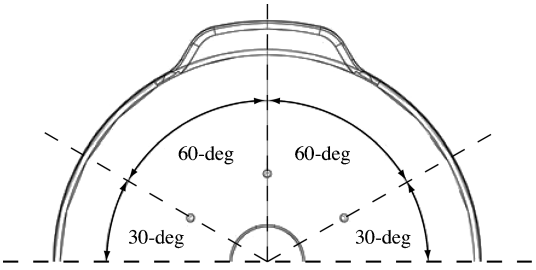

a) T-5-3B

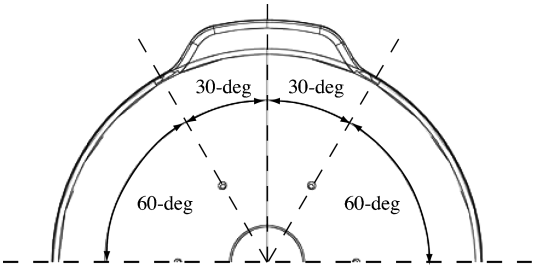

b) T-5-3C

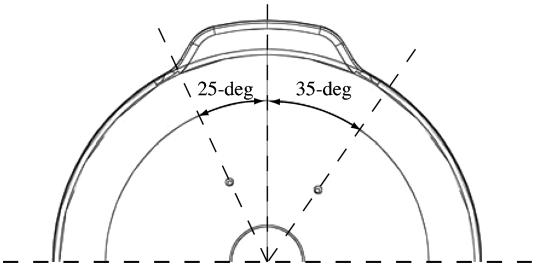

c) T-5-3D

Fig. 5 2007 MSL blended tab cavity configurations.

first cavity configuration, T-5-3B, had a cavity located on the model symmetry plane with the five other cavities located at 60-deg increments around the model. The second configuration, T-5-3C, had a cavity offset 30 deg to each side of the model symmetry plane with four other cavities located at 60-deg increments around the model. The final configuration, T-5-3D, had one cavity 25 deg off the symmetry plane and another cavity located 35 deg off the symmetry plane.

Throughout this report, reference will be made to windward and leeward surfaces of the forebody. The region above the nose in the forebody images will be referred to as the leeward side of the forebody; and the region below the nose in the forebody images will be referred to as the windward side of the forebody.

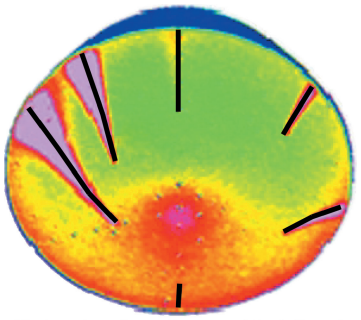

Fig. 6 Example data extraction lines.

(Data extractions shown as black lines.)

Data Reduction

One-dimensional, semi-infinite solid heat-conduction theory[14] was used to compute surface heating distributions from the global surface temperature data acquired through the technique of two-color, relative-intensity, phosphor thermography. A constant heat-transfer coefficient is assumed in this theory, and empirical corrections[14] are made to account for changes in model substrate thermal properties with temperature. Phosphor images were acquired shortly after injection of the model to the tunnel centerline, which requires less than 1 s.

Small, circular marks were placed on all models to aid in data reduction and model orientation. These fiducial marks do not influence the flow over the model surface. The fiducial marks can be seen in run images as dark dots and should not be confused with cavities.

Data cuts were extracted from the heat-transfer images. Example data extraction locations from the baseline configuration are given in Fig. 6. These locations are assumed to run along the streamline emanating from the cavities. Other data cuts were simply extracted along the symmetry plane. Results are presented herein in terms of a nondimensional heat-transfer coefficient ratio h/h_{FR}, where h_{FR} is the theoretical heating computed with the Fay–Riddell[16] method for a 0.0309-m sphere (which is the radius of the spherical portion of the nose of the test models) at 300 K. The heating ratios presented herein are not equal to one at the nose of the vehicle because the effective radius of the sphere cone is larger than the radius of the nose, which decreases the heating ratio. If the heating ratio is off scale in an image, it appears as a pink region (but is not out of the range of the phosphor system).

Error Analysis

The estimated experimental uncertainty of the thermographic phosphor system is a function of fluorescent intensity, which is dependent on model surface temperature. For higher temperatures (greater than 400 K), such as those of the forebody, the uncertainty[14] is approximately $\pm 8\%$ to $\pm 10\%$, whereas for lower temperatures (less than 325 K), such as those on the afterbody, the uncertainty is approximately ± 15 to $\pm 20\%$. Additional measurement uncertainty can be introduced as a result of heat conduction in high-gradient regions such as the shoulder of the vehicle. This uncertainty is estimated to vary from less than $\pm 5\%$ at the lowest test Reynolds numbers to greater than $\pm 10\%$ at the highest Reynolds numbers.

Uncertainties can be introduced when extracting line-cut data from an image as a result of perspective distortion of the image, lack of pixel resolution in high-gradient regions, and lack of precision in locating the fiducial marks. These errors are estimated to be less than $\pm 5\%$ on relatively flat surfaces and up to $\pm 10\%$ on highly curved surfaces.

A square root of the sum-of-the-squares estimate for the total uncertainty based on the preceding factors gives a worst-case experimental uncertainty range of $\pm 13\%$ on flat areas of the forebody to $\pm 25\%$ on the afterbody at high Reynolds numbers. In addition to the sources of experimental uncertainty just listed, additional uncertainty can also be introduced by early or asymmetric transition as a result of model surface roughness, including cavity rim roughness. The onset of transition is influenced by the roughness of the model surface, which tends to degrade slightly over the length of a test

because of handling of the model and pitting of the model surface from particle impacts. Some variation in the roughness of the phosphor coating from model to model can also be expected. Because this uncertainty increases over time and varies from model to model, no fixed value for the uncertainty is assigned. Instead, if anomalous results are noted when viewing trends in the heating data, such as in the Reynolds-number effects, the respective run images should be examined for signs of early or asymmetric transition.

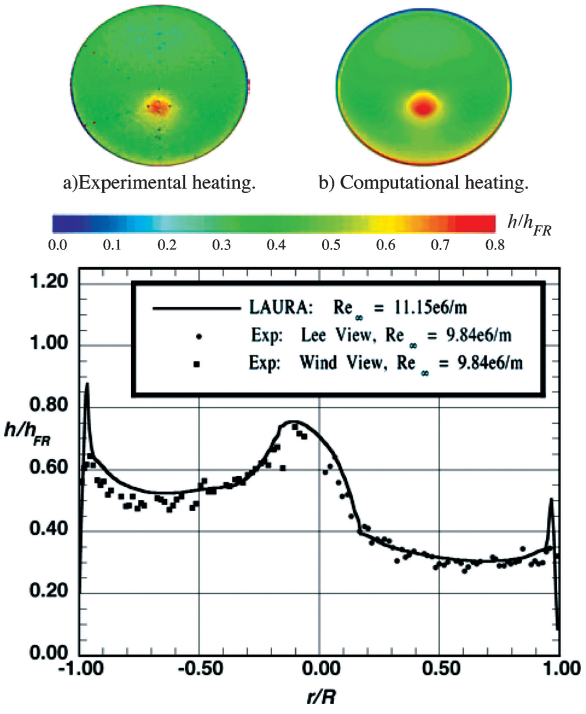

Fig. 7 Comparison of experimental and computational results at $Re_\infty = 9.84 \times 10^6$/m and $\alpha = 16$ deg.

Test Matrix and Tunnel Conditions

The data were collected at angles of attack of 0, 11, 16, and 20 deg, a sideslip angle of 0 deg, and freestream Reynolds numbers between 6.89×10^6/m and 23.95×10^6/m. The nominal and achieved test conditions are presented in Table 1. Although the test gas and flight gas are dissimilar, the boundary-layer-edge conditions are similar[9] and the wind-tunnel reproduced values of Re_D the vehicle will experience through its trajectory (see Fig. 3).

Flowfield Computations

Computational Method

Computations were performed using the LAURA[7,8] code (version 4.9.2). The LAURA code is a three-dimensional, finite volume solver, which includes perfect-gas, equilibrium, and nonequilibrium chemistry models. The code can be used to solve the inviscid, thin-layer Navier–Stokes or full Navier–Stokes equations. For the current study the thin-layer mode was employed; it was concluded in Ref. 2 from computations on the GSRC that this mode provided accurate results for attached forebody flows. Time integration to steady state in LAURA is accomplished through a point-relaxation scheme. Roe averaging[17] with Harten's entropy fix[18] and Yee's symmetric total-variation-diminishing limiter[9] is used for inviscid fluxes, and a second-order scheme is employed for viscous fluxes. In this study, the perfect-gas air model was used.

Freestream conditions for the LAURA wind-tunnel computations were set to the nominal freestream operating conditions of the NASA Langley 20-Inch Mach 6 Air Tunnel, which are listed in Table 1. For the computations, a uniform, ambient 300 K wall temperature boundary condition was imposed. The use of a constant wall temperature is valid because the experimental data are reported in terms of the nondimensional ratio h/h_{FR}, which is assumed to remain constant with wall temperature.

A structured, finite volume, multiple-block grid with a singularity-free nose block was employed for the 2007 MSL computations. The grid blocks contained approximately 230,000 points with a body-normal (k-index) resolution of 65 points. Grid adaptation was performed (as per the method detailed in Ref. 8) to align the

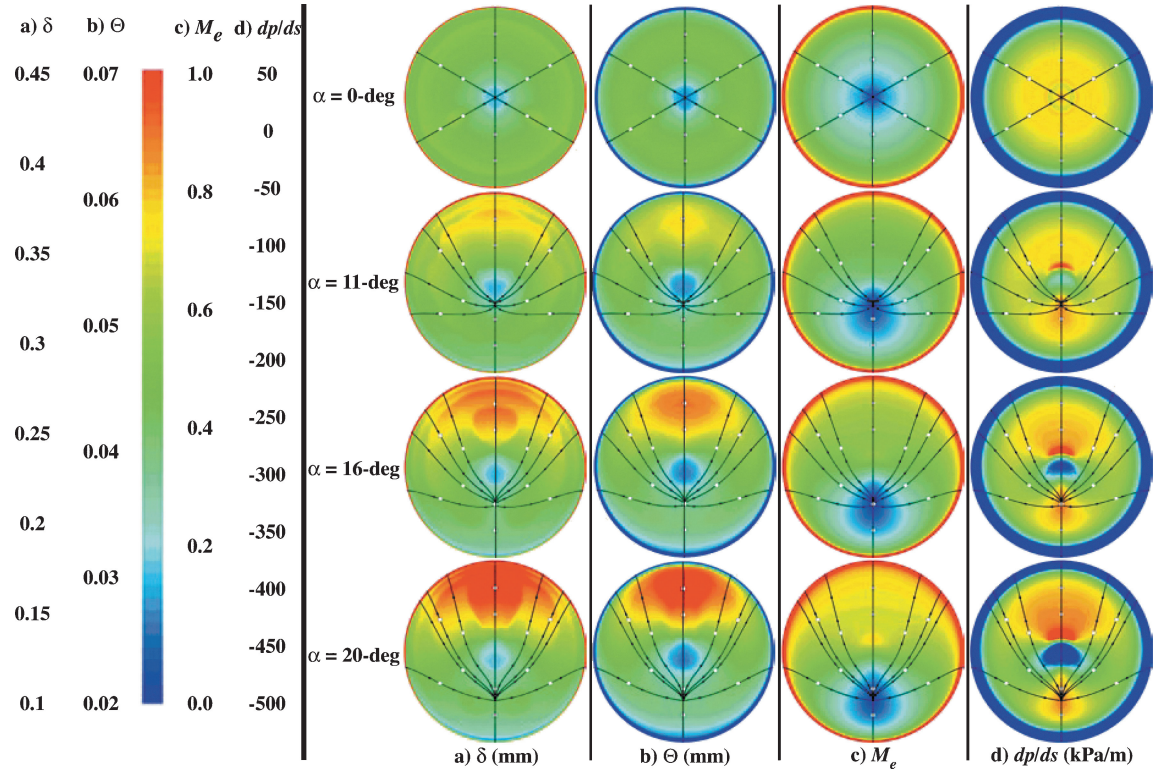

Fig. 8 Effect of angle of attack on boundary-layer properties at $Re_\infty = 9.84 \times 10^6$/m.

grids with the bow shock and to produce nominal wall cell Reynolds numbers on the order of $Re_{\text{cell}} = 10$.

A comparison between measured experimental heating and computational heating predictions for the 2007 MSL can be seen in Fig. 7. The computed laminar heating distribution agreed with the experimental data to within the estimated uncertainty. For a complete discussion of computational comparisons to the current experimental aeroheating data and the development of the transition correlation, see Ref. 9.

Boundary-Layer Analysis

To evaluate 2007 MSL boundary-layer properties, an algorithm was written to postprocess the LAURA output files in order to extract boundary-layer-edge conditions. The boundary-layer height δ was defined as the distance along the wall surface normal at which the stagnation enthalpy was equal to 99.5% of the freestream value. Flow properties were interpolated at discrete points along the wall surface normal, and a numerical integration was performed to calculate the boundary-layer momentum thickness Θ. The streamwise

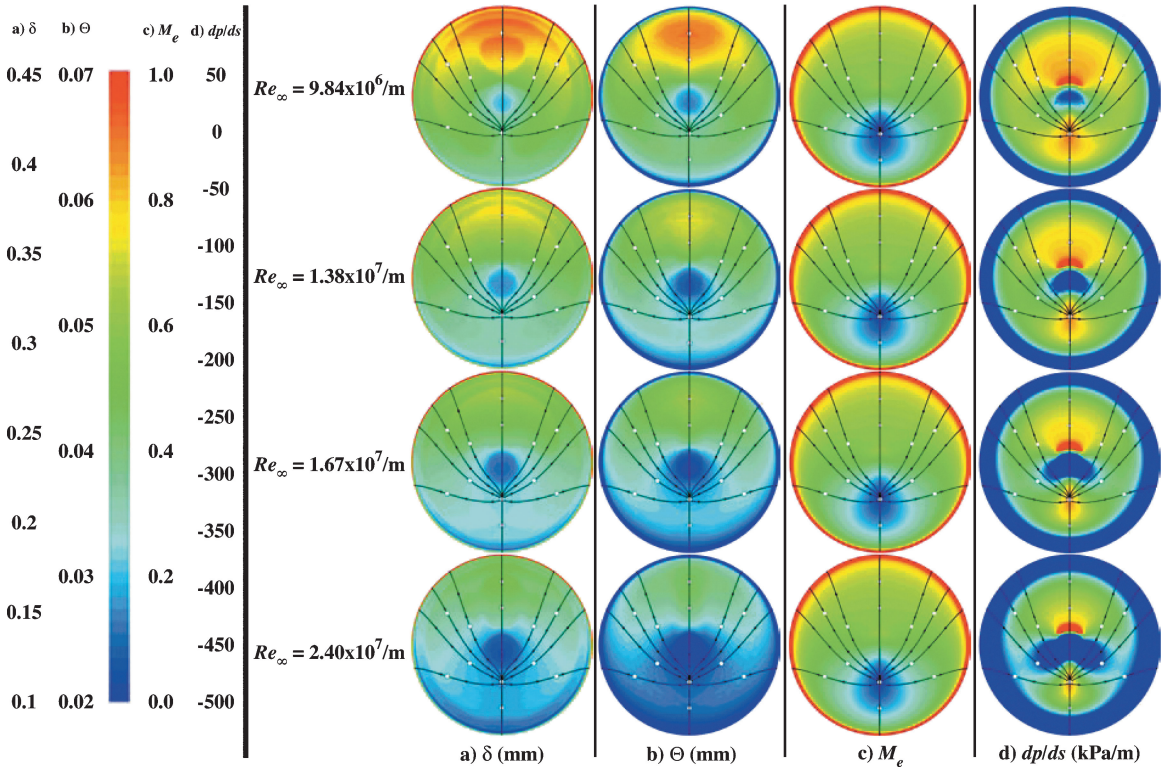

Fig. 9 Effect of freestream Reynolds number on boundary-layer properties at $\alpha = 16$ deg.

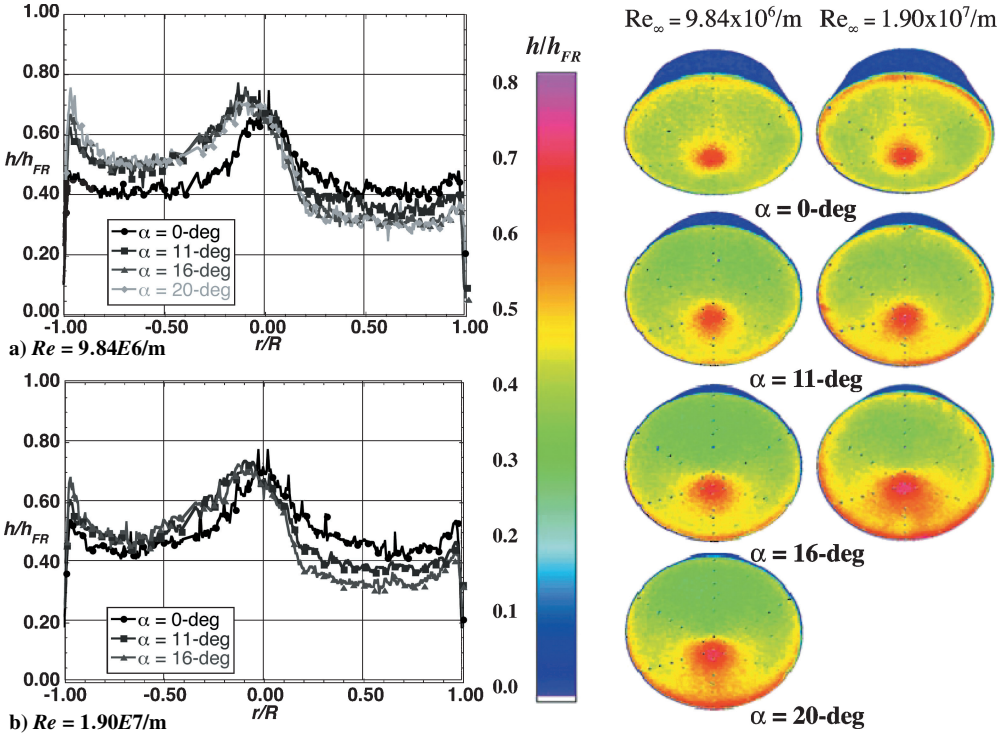

Fig. 10 Smooth model centerline heating and images.

pressure gradient and Mach number were also calculated at the boundary-layer edge. Boundary-layer-edge quantities such as these are used in Ref. 9 to formulate the boundary-layer transition criteria. Sample results are shown in Figs. 8 and 9.

As the angle of attack was increased, the stagnation point moves off the spherical nose onto the windward conic section of the forebody (Fig. 8). The boundary-layer height on the windward surface of the forebody decreased as angle of attack was increased, while increasing on the leeward surface of the forebody (Fig. 8). The momentum thickness on the windward surface of the forebody decreased as angle of attack increased, while increasing on the leeward surface (see Fig. 8). The boundary-layer-edge Mach number increased on the leeward surface of the forebody and decreased on the windward surface as angle of attack was increased, in general (Fig. 8). The edge Mach number of the 2007 MSL never exceeded 1.0, except at the shoulder. The streamwise pressure gradient increased along most of the symmetry plane as angle of attack was increased (especially just downstream of the geometric symmetry axis and near the stagnation point), but decreased just upstream of the geometric symmetry axis and along rays approximately 60 deg off of the windward centerline (Fig. 8).

As the Reynolds number was increased, both the boundary-layer height and momentum thickness decreased over the entire forebody (Fig. 9). The edge Mach number remained approximately constant (decreased slightly; Fig. 9). The streamwise pressure gradient decreased over all of the forebody as the Reynolds number was increased, except directly downstream of the geometric symmetry axis (Fig. 9).

Experimental Results

Forebody of Baseline Smooth Configuration

The nondimensional heating data from the smooth baseline 2007 MSL model are plotted along the model centerline (Fig. 10). The data are plotted vs the nondimensional distance ratio r/R, where r is the radial distance from the geometric center of the model and R is the maximum radius.

All data collected on the smooth baseline 2007 MSL model are believed to be laminar. The heating ratio h/h_{FR} near the nose varied from approximately 0.68 at 0-deg angle of attack to approximately 0.72 at 20-deg angle of attack. This was generally the location of highest heating on the forebody, the exception being the windward shoulder at 20-deg angle of attack.

The heating ratio on the leeward surface decreased to values ranging from approximately 0.28 to 0.40 as angle of attack decreased from 20 to 0 deg and remained at these levels to the shoulder. Heating levels began to rise as the flow reached r/R of approximately 0.9. The rapid expansion of the inviscid flow around the corner forms a large favorable pressure gradient, which results in a reduction of the boundary-layer thickness. This increased heating near the shoulder increased with Reynolds number because of a further decrease in boundary-layer height.

The heating ratio on the conical portion of the windward surface decreased to approximately $h/h_{\mathrm{FR}} = 0.50$ for all nonzero angles of attack ($h/h_{\mathrm{FR}} = 0.40$ for $\alpha = 0$ deg), then increased to between $h/h_{\mathrm{FR}} = 0.46$ at $\alpha = 0$ deg up to $h/h_{\mathrm{FR}} = 0.75$ at $\alpha = 20$ deg near the shoulder because of the expansion of the flow around the corner to the vehicle afterbody.

Forebody of Baseline Cavity Parametric Configuration

The nondimensional heating data from the cavity parametric models were plotted (Fig. 11) beginning at the cavity centers and continuing along the center of the transitional/turbulent wedge, which extended downstream from the cavity to the shoulder, and are assumed to correspond to a surface streamline. When a cavity did not produce a wedge of increased heating, the cut locations were determined from a run that did trip the flow. The heating data are plotted vs the nondimensional distance s/R, which is the wetted distance from the center of the cavity over the surface of the model to the shoulder of the model nondimensionalized by the model radius. Although heating data from within the cavities were not acquired, the downstream effects were studied. A cavity's ability to influence

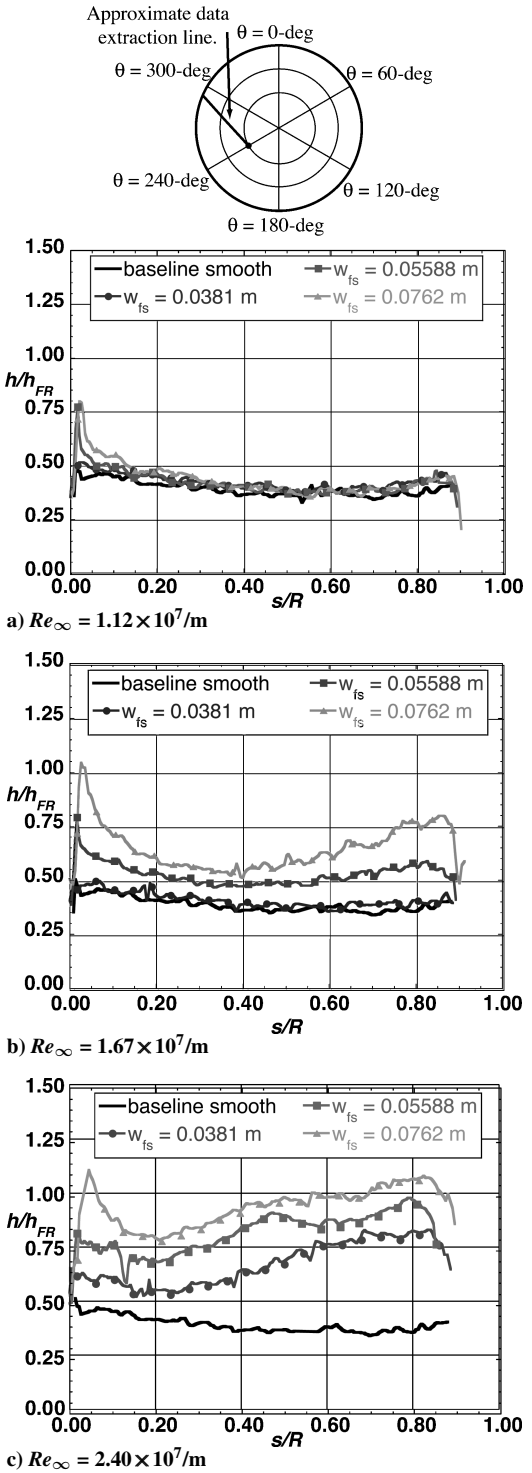

Fig. 11 Effect of cavity diameter at $\alpha = 16$ deg and $\theta = 240$ deg.

these parameters will be referred to as its effectiveness. Only a small subset of the database is presented herein.

The presence of a cavity can result in high, localized heating at the downstream edge of the cavity because of flow separation and reattachment within the cavity and can be accompanied by viscous effects downstream of its location (i.e., boundary-layer transition).

The larger the cavity size, the greater the effect on both local heating and the state of the boundary layer (see Fig. 11). The effectiveness of the cavities ranged from little or none up to an increase in localized heating levels of approximately 250% and in downstream heating levels of approximately 325% for $Re_\infty = 23.95 \times 10^6$/m (Fig. 11).

As Reynolds number was increased, the effectiveness of a cavity, regardless of its size, location, or the model angle of attack, increased

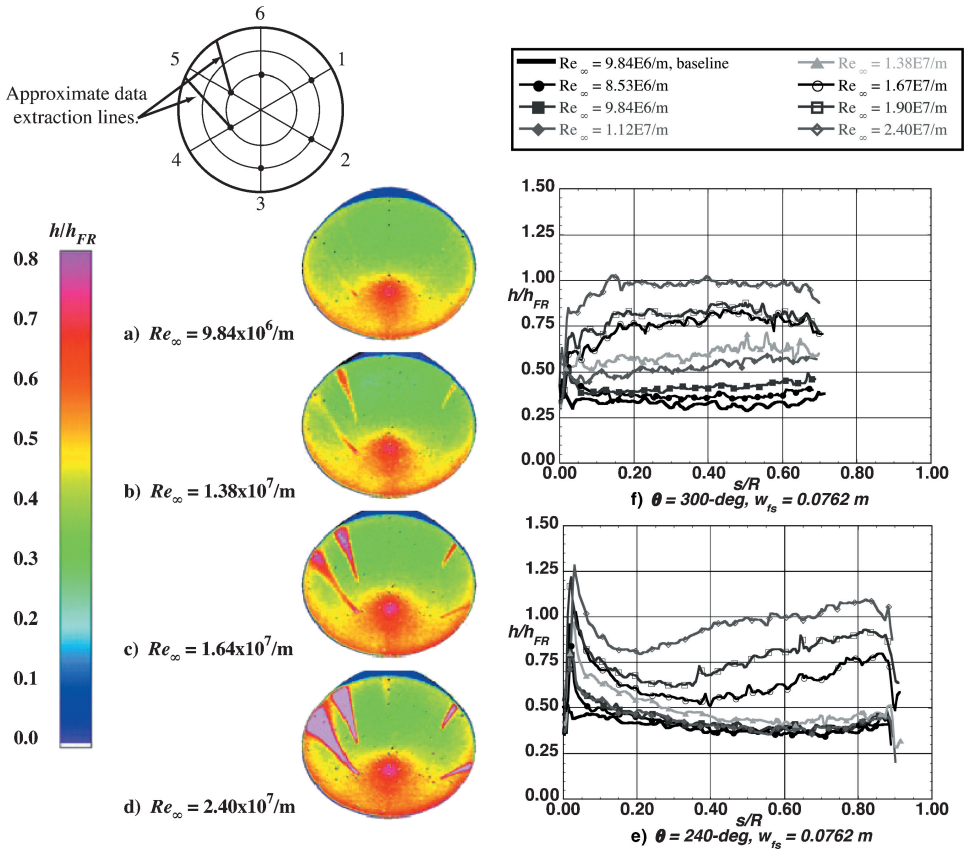

Fig. 12 Effect of Re_∞ for $\alpha = 16$ deg and $\phi = 300$ deg.

(Fig. 12). This is because the height of the boundary layer and momentum thickness decreased as Re_∞ increased. As the ratio of the characteristic dimension of a disturbance (cavity size) to the characteristic height of the boundary layer (height or momentum thickness) increases, the more effect the disturbance will have on the state of the boundary layer.

As angle of attack was increased, the effectiveness of a cavity was strongly influenced by its location on the forebody. Cavities that became more effective were located at both radial locations for $\theta = 120$ and 240 deg and at $r/R = 0.41$ for $\theta = 60$ and 300 deg (Fig. 13). These locations correspond to regions at which both δ and Θ either remained constant or decreased slightly as angle of attack increased. The cavities that became less effective were located at both radial locations at $\theta = 0$ deg and at $r/R = 0.70$ at $\theta = 60$ and 300 deg (Fig. 13). These locations correspond to regions at which δ and Θ were increasing with angle of attack. The windward centerline cavities remained essentially ineffective over the angle-of-attack range studied. A local increase in heating levels was observed, but no downstream effect was recorded.

When a cavity caused the boundary layer to become transitional for the nonzero angles of attack studied, there were two distinct trends the downstream heating levels followed. The first trend was an immediate increase in the heating level, followed by a gradual decrease and then gradual increase with s/R for higher Reynolds numbers (Fig. 12e). This was interpreted as an immediate tripping of the boundary layer to transitional/turbulent, followed by a gradual relaminarization (with further transition occurring at higher Reynolds numbers). Cavities exhibiting this behavior were located at both radial locations at $\theta = 120$, 180, and 240 deg at all angles of attack, as well as at $r/R = 0.41$ at $\theta = 60$ and 300 deg at $\alpha = 11$ deg. These locations correspond to regions where δ and Θ were relatively low (compared to the second pattern) and the downstream pressure gradients were strongly negative. The second trend was an immediate, relatively small increase in heating downstream of the cavity followed by a gradual increase in heating levels (see Fig. 12f). This was interpreted as a small initial disturbance introduced into the

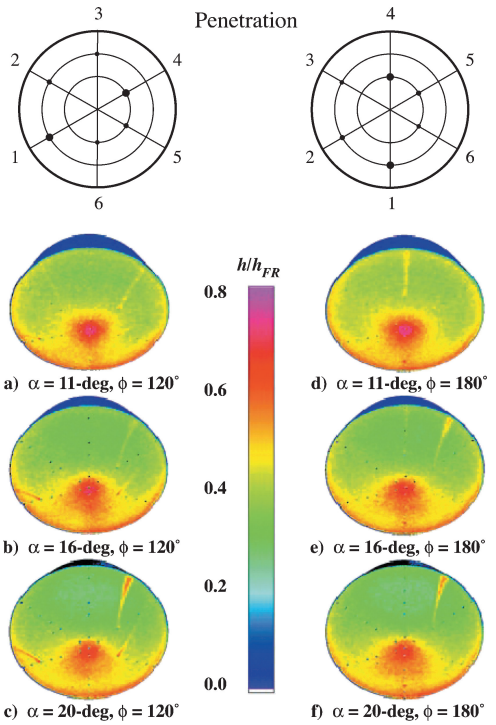

Fig. 13 Effect of angle of attack for $Re_\infty = 1.12 \times 10^6$/m at $\phi = 180$ deg.

boundary layer, followed by a transition toward turbulence. Cavities exhibiting this behavior were located at both radial locations at $\theta = 0$ deg and at $r/R = 0.70$ at $\theta = 60$ and 300 deg at all angles of attack. The $r/R = 0.41$, $\theta = 60$ and 300 deg locations were included in this pattern at $\alpha = 11$ deg. These locations correspond to regions where δ and Θ were relatively large (compared to the first pattern) and the downstream pressure gradients were greater than those of the first pattern.

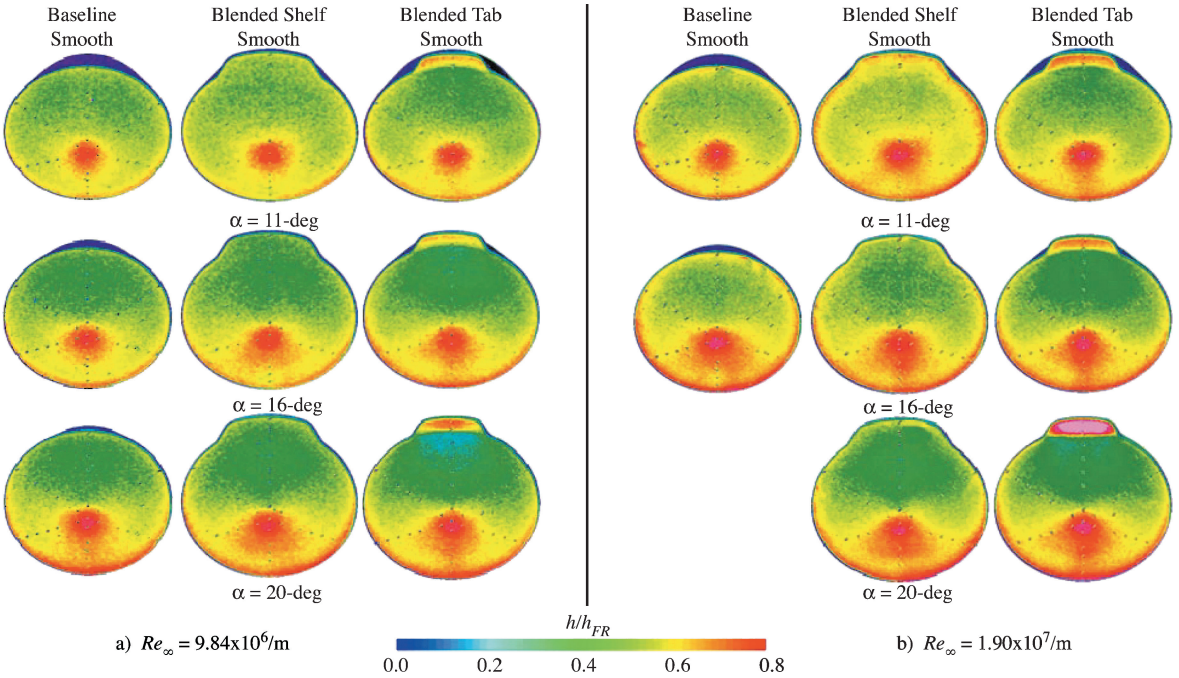

Fig. 14 Smooth 2007 MSL configurations global aeroheating images.

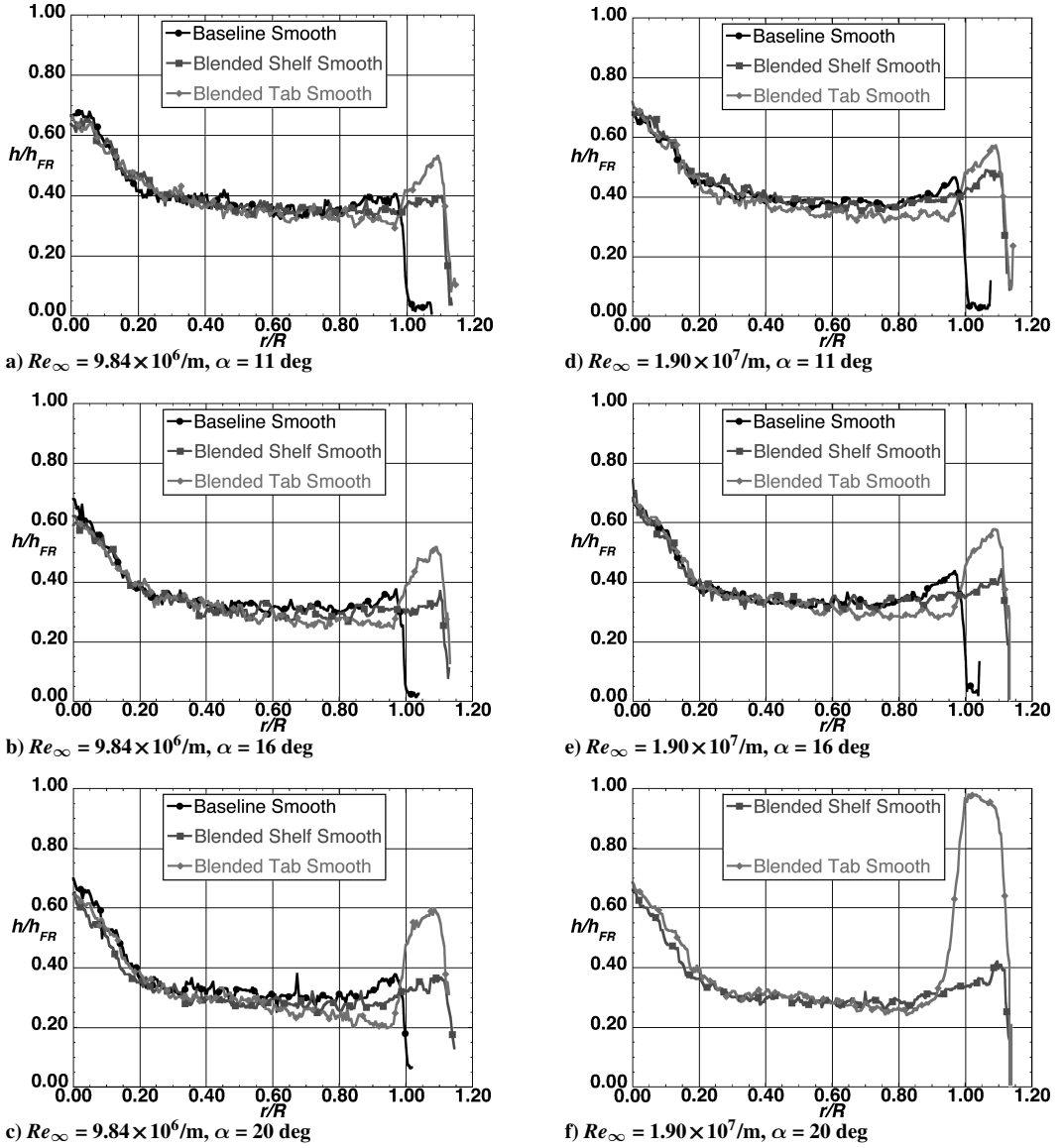

Fig. 15 Smooth 2007 MSL configurations centerline heating.

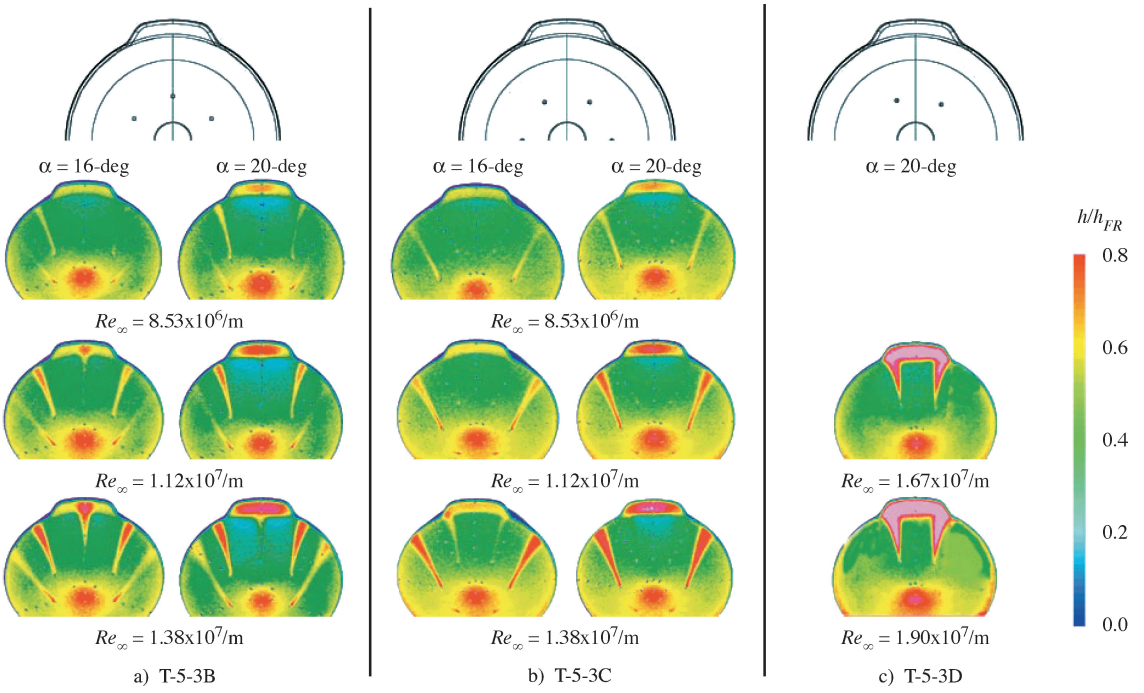

Fig. 16 Effect of Re_∞ and α on blended tab cavity configurations.

Forebody of Control Surface Smooth Configurations

Heating images for the smooth 2007 MSL control surface models (no cavities or discrete trips) are shown at $Re_\infty = 9.84 \times 10^6$/m and $Re_\infty = 1.90 \times 10^7$/m in Fig. 14. The corresponding centerline heating ratio h/h_{FR} is plotted vs the nondimensional distance ratio r/R in Fig. 15.

The presence of the blended shelf had little effect on the centerline heating distribution. The only effect it had was to increase the running length compared to the baseline model. The increase in heating attributed to the expansion of the flow around the corner of the baseline configuration is simply moved outboard to the corner of the blended shelf.

The blended tab, which was offset 10 deg into the flow from the forebody, produced a compression surface, which created a separation region upstream of the hinge line and increased the heating levels on the surface of the blended tab. At the lowest Reynolds number ($Re_\infty = 9.84 \times 10^6$/m; Figs. 15a–15c), the size of the separation region increased with angle of attack. The heating ratio on the blended tab increased with angle of attack, which might at first seem counterintuitive because the blended tab became more oblique to the freestream flow because it was on the leeward surface. However, because the size of the separation region was increasing with angle of attack, it was more likely to reattach in a transitional state, thereby increasing the heating ratio. At the highest Reynolds number ($Re_\infty = 1.90 \times 10^7$/m; Figs. 15d–15f), the size of the separation region upstream of the blended tab decreased compared to the $Re_\infty = 9.84 \times 10^6$/m cases. The trend of increasing heating rates on the blended tab as angle of attack was increased was augmented for the $\alpha = 20$-deg case at the higher Reynolds number. The transitional reattachment at this angle of attack increased the heating ratio on the blended tab by approximately 160%.

Forebody of Control Surface Cavity Configurations

It has been shown herein that the cavities located on the leeward side of the forebody of the proposed 2007 MSL are more likely to cause boundary-layer transition than those on the windward side. Because of this, the effects of cavity placement on blended tab heating were studied at varying angles of attack and Reynolds numbers.

The cavities that influence heating levels on the blended tab must first be identified. Figures 16a and 16b show model configurations T-5-3B and T-5-3C, respectively, at $\alpha = 16$ and 20 deg and $Re_\infty = 8.53 \times 10^6$/m, 1.12×10^7/m, and 1.38×10^7/m. Figure 16c shows model T-5-3D at $\alpha = 20$ deg and $Re_\infty = 1.67 \times 10^7$/m and 1.90×10^7/m. The cavities located 60 deg or more off the leeward centerline did not affect the heating rates on the blended tab at either angle of attack tested, while those offset 30 deg from the centerline did at $\alpha = 16$ deg at the highest Reynolds number. The cavities offset 25 and 35 deg off of the leeward centerline did affect heating on the blended tab at $\alpha = 20$ deg.

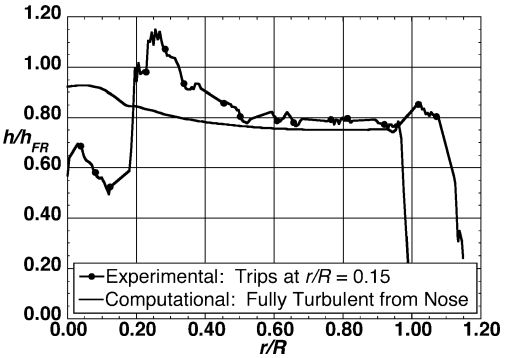

Fig. 17 Comparison of experimental (tripped) and computational (fully turbulent) flow at $Re_\infty = 1.90 \times 10^7$/m and $\alpha = 16$ deg.

At $\alpha = 16$ deg, the leeward centerline cavity (Fig. 16a) and the cavities located 30 deg off centerline (Fig. 16b) had an effect on local aeroheating for the blended tab for the Reynolds numbers tested. However, at $\alpha = 20$ deg (right-hand columns in Figs. 16a and 16b), by the time the cavities became effective, the separated shear layer in front of the tab was already transitional, so that the heating on the blended tab was already elevated.

It is recommended that the cavities be placed 30 deg off of the leeward centerline and then at 60-deg intervals around the forebody, as configuration T-5-3C (Fig. 16b) demonstrates. This is suggested because the cavity on the leeward centerline is more effective than those placed 30 deg off of the centerline, causing higher heating for a given Reynolds number.

The effect a cavity on the leeward centerline had on blended tab heating rates and distributions will now be examined. These data for a cavity will be compared to data without cavities but with discrete trips placed near the leeward sphere-cone juncture ($r/R = 0.15$)

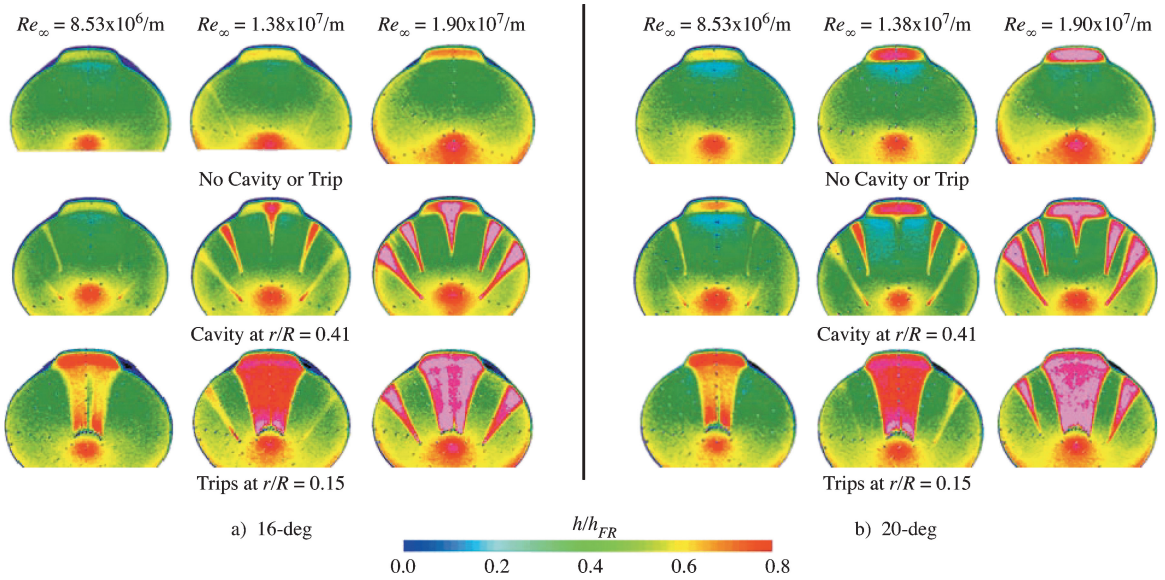

Fig. 18 Effect of cavities and discrete trips on blended tab configuration.

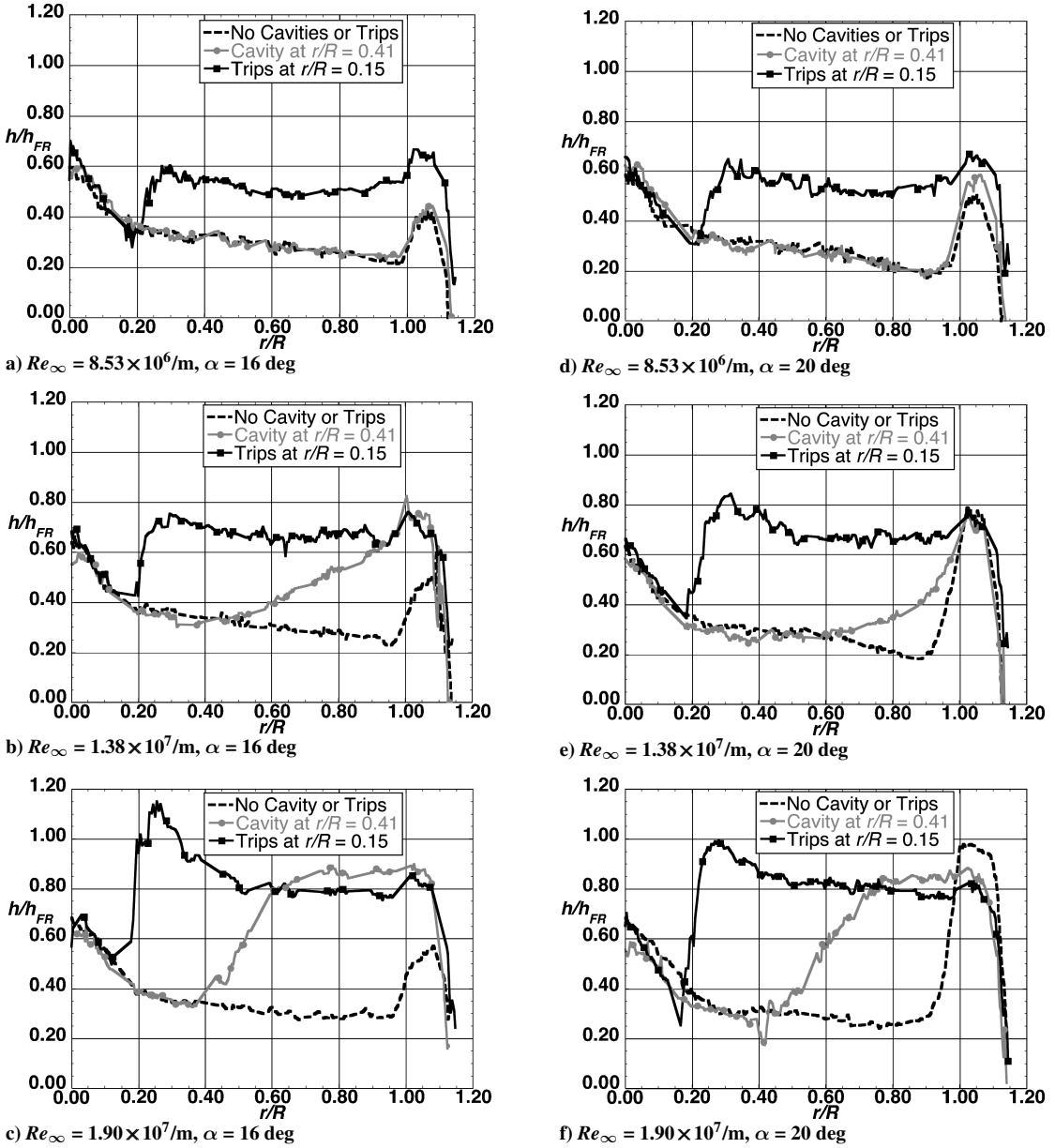

Fig. 19 Effect of cavities and discrete trips on leeward centerline heating for blended tab configuration.

of the model. The results with discrete trips are included to provide fully turbulent cases for comparison to the transition results corresponding to the presence of the cavity. A comparison of the discrete trip data on the blended tab configuration and a fully turbulent computation[9] on the baseline configuration at $\alpha = 16$ deg, $Re_\infty = 1.90 \times 10^7$/m is shown in Fig. 17. The discrete trip has an initial overshoot downstream of the trip compared to the computation. This is attributed to the effects of the presence of the trip such as a local shock and vortices generated by the trip. The boundary layer is typically referred to as fully developed turbulent flow when a "plateau" is reached (located at approximately $r/R = 0.5$ in Fig. 17). This plateau compares within experimental uncertainty with the prediction.

Global heating distributions for a range of Reynolds numbers are shown in Fig. 18a at $\alpha = 16$ deg and in Fig. 18b at $\alpha = 20$ deg. Corresponding leeward centerline data are plotted in Figs. 19a–19c and 19d–19f, respectively. In general, as the Reynolds number was increased the heating ratio downstream of the cavities and discrete trips increased. At the lowest Reynolds number (Figs. 19a and 19d), the cavity had no effect on the heating ratio compared to the smooth blended tab on the forebody of the model. The $\alpha = 20$-deg blended tab heating, however, did increase slightly.

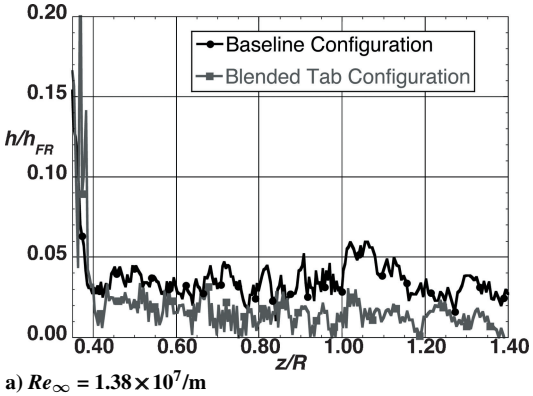

a) $Re_\infty = 1.38 \times 10^7$/m

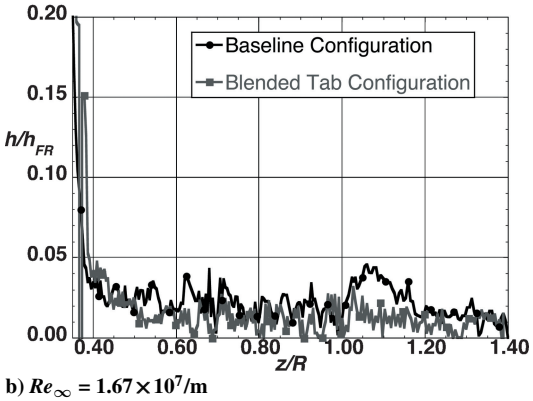

b) $Re_\infty = 1.67 \times 10^7$/m

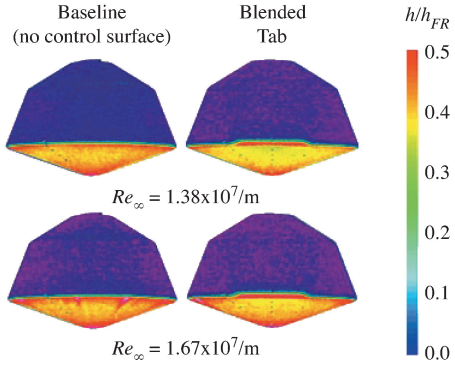

c) Global heating image

Fig. 20 Leeward afterbody heating at $\alpha = 11$ deg.

For the $\alpha = 16$-deg data (Figs. 19a–19c), the tripped blended tab heating distributions were approximately 50% higher than the laminar blended tab heating distributions over the Reynolds-number range tested. At $\alpha = 20$ deg, however (Figs. 19d–19f), the separated shear layer for the smooth blended tab configuration becomes transitional/turbulent, especially at the higher Reynolds numbers tested (Fig. 19f). The smooth blended tab model heating was actually higher than those from the tripped blended tab model. This elevation in untripped downstream boundary-layer heating rates on control surfaces tested in ground facilities has been observed for X-33 body flap heating[19] and is believed to be caused by the tripped, thicker boundary layer reattaching the deflected surface earlier, resulting in a smaller separation region and lower turbulent reattachment heating levels. The laminar separation yields flow reattachment that is transitional and heating that is characteristically higher than turbulent results.

When the flow downstream of a cavity did become fully turbulent (Figs. 19c and 19f), the plateau reached was above that of the fully turbulent tripped data. This is attributable to both local effects from

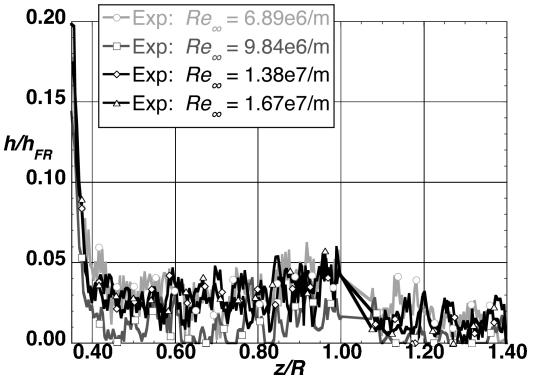

a) $\alpha = 11$ deg

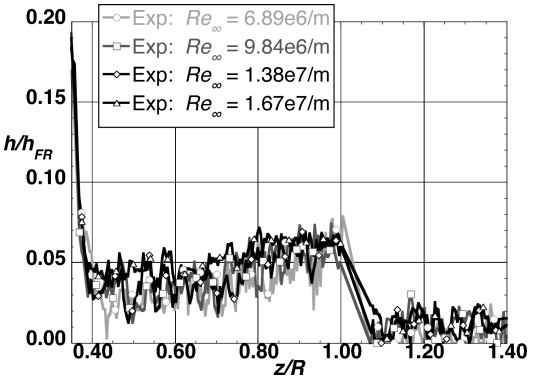

b) $\alpha = 16$ deg

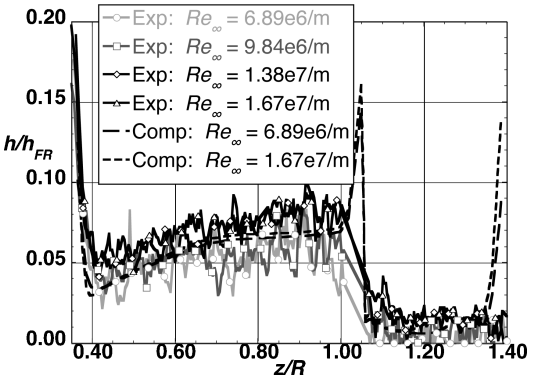

c) $\alpha = 20$ deg

Fig. 21 Windward afterbody centerline heating distribution.

the presence of the cavity (as discussed earlier with the discrete trip) and because of the increased running length upstream of the cavity. The boundary-layer thickness at the cavity was greater than that at the discrete trip. For a detailed discussion on computed turbulent levels and comparison to the baseline configuration, see Ref. 9.

Effect of Cavities and Control Surfaces on Leeward Afterbody Heating

Leeward afterbody heating images for both the baseline and blended tab configurations are shown in Fig. 20c for an angle of attack of 11 deg. (Note that the color scale has been decreased from a maximum of $h/h_{FR} = 0.8$ to $h/h_{FR} = 0.5$.) This angle of attack is taken as representative of the three angles tested. The other two (16 and 20 deg) are similar. The corresponding centerline nondimensional heating data are shown in Figs. 20a and 20b. Heating data are plotted vs the nondimensional distance z/R, where $z/R = 0.38$ is the location of the corner of the baseline configuration. The uncertainty in this data was approximately $\pm 25\%$ because of the much smaller increase in surface temperature than which was measured on the forebody during a run. All heating ratios were below $h/h_{FR} = 0.05$, which was significantly lower than those of the forebody. There is also a slight difference between the afterbody heating for the baseline configuration compared to the blended tab configuration. The blended tab configuration heating levels were generally lower than those of the baseline configuration.

For the cases when the forebody cavities tripped the boundary layer, the boundary layer relaminarized at the corner because of the strong negative pressure gradient. Thus, the cavities had no effect on leeward afterbody heating.

Windward Afterbody Heating

Windward afterbody centerline heating distributions are shown in Fig. 21. Heating data are plotted vs the nondimensional distance z/R. Once again, the temperature rise during a run was small compared to that of the forebody, so that the error was approximately $\pm 25\%$. As angle of attack was increased from 11 to 20 deg, the heating ratio on the windward centerline increased. An increase in heating was also seen as Reynolds number increased, especially at $\alpha = 20$ deg. A comparison to computations is included for the $\alpha = 20$-deg case in Fig. 21c. Good agreement (well within the $\pm 25\%$ uncertainty) between prediction and experiment was achieved.

Conclusions

An experimental aeroheating study was conducted on the Mars Science Laboratory aeroshell in the NASA Langley 20-Inch Mach 6 Air Tunnel using the technique of phosphor thermography. This test was conducted to determine whether heat-shield cavities had an impact on forebody heating, to determine the aeroheating characteristics for several control surface configurations (the blended shelf and blended tab), and to determine the effects of forebody cavities had on control surface heating distributions and levels. The afterbody heating was also examined to determine what, if any, impact the cavities and control surfaces had on the afterbody environment.

This study was complemented by an analysis of boundary-layer quantities obtained from thin-layer, laminar, Navier–Stokes flowfield solutions. The computational results quantified the boundary-layer height, momentum thickness, edge Mach number, and streamwise pressure gradient as functions of freestream Reynolds number, angle of attack, and location on the aeroshell forebody.

Baseline configuration cavity parametric model heating data showed that the effectiveness of a cavity depended on the cavity diameter, boundary-layer height, and momentum thickness. As the cavity diameter increased, the effectiveness of the cavity increased. As the boundary-layer height decreased, the effectiveness of a cavity increased. The presence of a cavity was shown to cause the increase in local heating levels by as much as 250% and downstream heating levels by as much as 325% because of boundary-layer transition.

The presence of the blended shelf had little effect on the proposed 2007 MSL aeroshell forebody heating. The only effect it had was to increase the running length compared to the baseline model (no control surface). The blended tab, which was offset 10 deg into the flow from the forebody, produced a compression surface and created a separation region upstream of the hinge line, which increased the heating levels on the surface of the blended tab. At the highest value of Reynolds number tested and 20-deg angle of attack, the separated shear layer reattached transitionally, causing heating rates greater than those at the nose of the vehicle.

The cavity locations that influence heating levels on the blended tab were identified for a radial location of $r/R = 0.41$. It was found that cavities offset 60 deg or more off of the leeward centerline did not impact blended tab heating for the angles of attack studied, but, cavities up to at least 35 deg off of the leeward centerline did.

Blended tab heating levels were studied for several cavity and discrete trip configurations. Discrete trips located at $r/R = 0.15$ caused the boundary layer to transition immediately, resulting in an overshoot in the heating ratio, followed by fully turbulent heating. For the highest Reynolds number, fully turbulent heating levels were reached, but were higher than the tripped fully turbulent case because of the increase in running length and local effects from the cavity.

For the cases where the boundary layer was tripped upstream of the blended tab, heating was generally higher than for the untripped cases, the exception being at an angle of attack of 20 deg for the highest Reynolds number, where the smooth configuration experienced higher tab heating levels as a result of the transitional reattachment heating levels being higher than the turbulent levels.

Afterbody heating levels were examined to determine the effects of the presence of the cavities and control surfaces. It was found that the forebody cavities had negligible effects on afterbody heating, and control surfaces decreased leeward afterbody heating slightly.

The study concluded that forebody cavities did indeed have an impact on heating levels of the Mars Science Laboratory by augmenting local and downstream heating. These results contributed to the decision to eliminate cavities from the design of the Mars Science Laboratory.

Acknowledgments

The authors acknowledge the contributions of the following individuals to this research: Jonny Ellis, Grace Gleason, and Roland Hatten for operation of the 20-Inch Mach 6 Air Tunnel and data-acquisition support; Joe Powers and Mark Griffith for fabrication of the ceramic test models; Mary Kae Lockwood for programmatic support; Mark McMillin for generating the CAD files necessary to fabricate the models; and Kathy Kuykendoll for model fidelity measurements and fiducial mark placement.

References

[1]Lockwood, M. K., and Graves, C. A., "Entry System Design Considerations for Mars Landers," American Astronautical Society, Paper 01-023, Jan.–Feb. 2001.

[2]Cheatwood, F. M., Merski, N. R., Riley, C. J., and Mitcheltree, R. A., "Aerothermodynamic Environment Definition for the Genesis Sample Return Capsule," AIAA Paper 2001-2889, June 2001.

[3]Sammonds, R. I., and Dickey, R. R., "Effectiveness of Several Control Arrangements on a Mercury-Type Capsule," NASA TM X-579, Oct. 1961.

[4]Prabhu, R. K., "Inviscid Flow Computations of Several Aeroshell Configurations for a '07 Mars Lander," NASA CR-2001-210851, April 2001.

[5]Prabhu, R. K., "Inviscid Flow Computations of Two '07 Mars Lander Aeroshell Configurations over a Mach Number Range of 2 to 24," NASA CR-2001-210852, April 2001.

[6]Edquist, K. T., Liechty, D. S., Hollis, B. R., Alter, S. J., and Loomis, M. P., "Aeroheating Environments for a Mars Smart Lander," *Journal of Spacecraft and Rockets*, Vol. 43, No. 2, 2006, pp. 330–339.

[7]Gnoffo, P. A., "An Upwind-Biased, Point-Implicit Algorithm for Viscous, Compressible Perfect-Gas Flows," NASA TP-2953, Feb. 1990.

[8]Cheatwood, F. M., and Gnoffo, P. A., "User's Manual for the Langley Aerothermodynamic Upwind Relaxation Algorithm (LAURA)," NASA TM-4674, April 1996.

[9]Hollis, B. R., and Liechty, D. S., "Transition Due to Heat-Shield Cavities on a Mars Entry Vehicle," *Journal of Spacecraft and Rockets*, Vol. 43, No. 2, 2006, pp. 354–366.

[10]Micol, J. R., "Langley Aerothermodynamics Facilities Complex: Enhancements and Testing Capabilities," AIAA Paper 98-0147, Jan. 1998.

[11]Buck, G. M., "Automated Thermal Mapping Techniques Using Chromatic Image Analysis," NASA TM 101554, April 1989.

[12]Buck, G. M., "Surface Temperature/Heat Transfer Measurement Using a Quantitative Phosphor Thermography System," AIAA Paper 91-0064, Jan. 1991.

[13]Merski, N. R., "A Relative-Intensity, Two-Color Phosphor Thermography System," NASA TM 104123, Sept. 1991.

[14]Merski, N. R., "Global Aeroheating Wind-Tunnel Measurements Using Improved Two-Color Phosphor Thermography Method," *Journal of Spacecraft and Rockets*, Vol. 36, No. 2, 1999, pp. 160–169.

[15]Buck, G. M., and Vasques, P., "An Investment Ceramic Slip-Casting Technique for Net-Form, Precision, Detailed Casting of Ceramic Models," U.S. Patent 5,266,252, Nov. 1993.

[16]Fay, J. A., and Riddell, F. R., "Theory of Stagnation Point Heat Transfer in Dissociated Air," *Journal of Aeronautical Sciences*, Vol. 25, No. 2, 1958, pp. 73–85.

[17]Roe, P. L., "Approximate Riemann Solvers, Parameter Vectors and Difference Schemes," *Journal of Computational Physics*, Vol. 43, No. 2, 1981, pp. 357–372.

[18]Harten, A., "High Resolution Schemes for Hyperbolic Conservation Laws," *Journal of Computational Physics*, Vol. 49, No. 3, 1983, pp. 357–393.

[19]Horvath, T. J., Berry, S. A., Hollis, B. R., Liechty, D. S., Hamilton, H. H., and Merski, N. R., "X-33 Experimental Aeroheating at Mach 6 Using Phosphor Thermography," AIAA Paper 99-3558, June/July 1999.

M. K. Lockwood
Guest Editor

Color reproductions courtesy of NASA Langley Research Center.